Journal of Applied Physics

RESEARCH ARTICLE | JULY 23 2025

Disorder driven magnetostructural coupling in $MnCoGe_{1-x}Sn_x$

M. Azavedo ; E. T. Dias ; K. R. Priolkar

J. Appl. Phys. 138, 043903 (2025)
https://doi.org/10.1063/5.0281364

Journal of Applied Physics ARTICLE pubs.aip.org/aip/jap

Disorder driven magnetostructural coupling in $MnCoGe_{1-x}Sn_x$

Cite as: J. Appl. Phys. **138**, 043903 (2025); doi: 10.1063/5.0281364
Submitted: 19 May 2025 · Accepted: 3 July 2025 ·
Published Online: 23 July 2025

M. Azavedo, E. T. Dias, and K. R. Priolkar[a)]

AFFILIATIONS

School of Physical and Applied Sciences, Goa University, Taleigao Plateau, Goa 403206, India

[a)]**Author to whom correspondence should be addressed:** krp@unigoa.ac.in

ABSTRACT

MnCoGe-based intermetallics have garnered significant attention owing to their pronounced negative thermal expansion and large magnetocaloric effect (MCE), both of which are highly sensitive to chemical substitutions. Despite extensive studies, the microscopic origin underlying the tunability of these properties remains unclear. In this study, we conducted a comprehensive investigation of the local atomic environments around Mn and Co in $MnCoGe_{1-x}Sn_x$ ($0 \leq x \leq 0.1$) using extended x-ray absorption fine structure and other structural and magnetic characterization techniques. Our analysis reveals that the substitutional disorder introduced by Sn atoms occupying the Ge sublattice sites disrupts the cooperative lattice distortions required for the long-range displacive martensitic transformation. This disorder-induced suppression results in a systematic decrease in both the martensitic transition temperature (T_M) and the magnetic ordering temperature (T_C). At low doping levels, the convergence of T_M and T_C enhances magnetostructural coupling, thereby amplifying the MCE. However, further Sn substitution ultimately suppresses the martensitic transition entirely, leading to a decoupling of the magnetic and structural degrees of freedom and a consequent degradation of the magnetostructural response.

I. INTRODUCTION

Stoichiometric MnCoGe has been primarily explored for its magnetocaloric and magnetovolume properties.[1–8] These properties originate from the underlying martensitic transformation at approximately $T_M = 420$ K from the paramagnetic (PM), austenitic Ni_2In-type hexagonal structure ($P6_3/mmc$) to PM, and martensitic TiNiSi-type orthorhombic structure (Pnma). The lattice constants of the two polymorphs are related as $a_{orth} = c_{hexa}$, $b_{orth} = a_{hexa}$, and $c_{orth} = \sqrt{3}a_{hexa}$. Accompanied by this structural transition is a large negative thermal expansion (NTE) of around 3.9%,[9–12] causing the sample to naturally break and powder upon cooling through the transition. On further cooling, MnCoGe undergoes a magnetic transition from the paramagnetic to the ferromagnetic state at $T_C \sim 345$ K,[13,14] giving rise to a large magnetocaloric effect (MCE). The ferromagnetic order is primarily due to the alignment of Mn spins along the c_{orth}-axis with a magnitude of $\sim 2.9\mu_B$. In the orthorhombic phase, Co atoms also possess a magnetic moment of $0.9\mu_B$.[15] The wide difference in structural and magnetic transition temperatures results in a weak magnetostructural coupling in MnCoGe.

To optimize magnetostructural coupling, different strategies have been employed to bridge the gap between T_C and T_M. These include altering the stoichiometry of MnCoGe,[16–19] substitutions at the Mn, Co, or Ge sites, and the introduction of interstitial atoms.[20–31] Such alterations in the composition of MnCoGe alloys have proved successful in enhancing the entropy change at the magnetostructural transition (ΔS_M) and the refrigeration capacity (RC) values, respectively, up to 48 J/kg K and 230 J/kg in a field change of 5 T,[18,19,29,31] which are comparable to other materials exhibiting giant MCE near room temperature.[32]

The average valence electron per atom (e/a) ratio and size of the substituted atoms for the chemical pressure effect have been the main considerations in implementing these approaches. A positive chemical pressure tends to stabilize the hexagonal phase and effectively tunes the T_M to below room temperature.[33–35] This stabilization is associated with the fact that the Mn–Mn bond distance in the hexagonal phase is shorter than that in the orthorhombic phase; hence, substitution with a smaller dopant atom reduces the Mn–Mn spacing and favors the formation of a hexagonal structure.[36–39] This is effectively demonstrated with the

introduction of 10 at. % Fe at the Mn site[33,34] However, substitution of Co by Fe also shows a similar effect.[35] Though the atomic radius of Fe lies between that of Mn and Co, with Mn being the larger, Fe substitution at both Mn and Co sites leads to a net reduction in unit cell volume, suggesting that the stabilization of the hexagonal phase may not be primarily driven by a chemical pressure effect. However, chemical pressure alone cannot fully account for the reduction in T_M observed when larger atoms such as In replace Co in MnCoGe. This argument is further strengthened by comparing results of Si (smaller atomic radius) and Sn (larger atomic radius) substitution at the Ge site in MnCoGe. Here, contrary to expectations, substitution of Si results in an increase in T_M while Sn substitution causes a decrease in T_M and T_C.[40,41]

Chemical bonding between the nearest Mn atoms in stabilizing the hexagonal phase is also considered an important factor. Antisite disorder and a decrease in valence electron count (VEC) of the alloy are shown to work counterintuitively in decreasing T_M and enhancing the magnetostructural coupling.[30,42,43] Substitution of Co atoms at the Mn site increases the total energy of the system leading to MnCoGe transforming martensitically at elevated temperature while a decrease in the VEC of the alloy tends to stabilize the hexagonal state of MnCoGe.

Another important parameter invoked to explain the behavior of T_M and T_C is the electron-to-atom (e/a) ratio of the alloy. Generally, a decrease in the e/a ratio of the alloy results in the suppression of T_M in MnCoGe and related alloys.[44–48] Further, the interplay between chemical pressure and the e/a ratio has also been explored through Al doping. Substitution of Ge with Al results in a simultaneous decrease in both T_M and T_C,[49] whereas Al substitution at the Mn site leads to an increase in T_C. These divergent trends are attributed to the dual effect of Al doping on both the interatomic distances between magnetic elements and the electronic structure, particularly the density of states (DOS) of the 3d electrons.[50] Similar results were obtained through a study involving In doping at the Co and the Ge sites.[43] In contrast, substitution of Ge by the smaller Si atom results in a concurrent increase in T_M and T_C,[51] while doping with the larger Sn atom reduces both T_M and T_C.[41] Another critical factor influencing the suppression of T_M is the electronegativity difference between the dopant and the host elements (Mn, Co, or Ge). The introduction of a less electronegative element at the Co site, or a more electronegative element at the Mn site, tends to strengthen Mn–Mn bonding, thereby lowering the martensitic transition temperature.[52–54] Similarly, substitution of Mn with non-magnetic Sn leads to a decrease in T_M and an increase in T_C, facilitating the emergence of a magnetostructural transition.[55]

Despite extensive studies, a unified mechanism underlying the modulation of T_M and T_C in MnCoGe-based alloys upon chemical doping remains elusive. In the present work, we systematically investigate the effect of Sn substitution at the Ge site in MnCoGe to elucidate the role of chemical modification at the non-magnetic atomic site on the structural, magnetic, and thermal expansion behaviors of the alloy. To probe the local atomic environmental changes induced by Sn doping, extended x-ray absorption fine structure (EXAFS) spectroscopy was employed as a function of temperature, with particular emphasis on the vicinity of the magnetostructural transition.

II. EXPERIMENTAL

Polycrystalline $MnCoGe_{1-x}Sn_x$ ($x = 0$, 0.025, 0.05, 0.075, 0.1) alloys were prepared by arc melting high purity (> 99.99%) Mn, Co, Ge, and Sn in an inert argon atmosphere. The sample was flipped 3–4 times during the melt to ensure homogeneity. The obtained ingot was then cut into pieces using low power diamond saw, and some of these pieces were finely powdered. The pieces and powder wrapped in tantalum foil were sealed in an evacuated quartz tube and annealed at 850 °C for 120 h followed by furnace cooling. The pieces of $x = 0$ crumbled into a fine powder upon annealing indicative of its first order transition temperatures to be above room temperature. X-ray diffraction (XRD) measurements were performed using a Rigaku x-ray diffractometer with Bragg–Brentano geometry in the 2θ range of 20°–100° with a step size of 0.02° using Cu K_α radiation. The stoichiometry and compositional homogeneity were verified by scanning electron microscopy with energy-dispersive x-ray spectroscopy (SEM-EDS) over a $100 \times 100\,\mu m^2$ area of the sample. In order to identify the structural transition temperatures, Differential Scanning Calorimetry (DSC) measurements were performed by employing Shimadzu DSC-60, at a rate of 5 K/min during the heating and cooling cycles in the temperature range of 120–450 K. A cryogenic S-700X SQUID magnetometer was employed for magnetization measurements. For the temperature dependent magnetization measurements (M(T)), the sample was cooled in zero applied field from 300 to 5 K. Magnetization was recorded in the temperature interval of 5–390 K while warming (zero field cooled, ZFC), subsequent cooling (field cooled cooling, FCC) and warming (field cooled warming, FCW) cycles in a field of 100 Oe. Isothermal magnetization (M(H)) measurements were performed in the field range from 0 to 7 T (One quadrant 1Q) at 5 K interval over a temperature range of 60 K around the T_C's of the respective alloys. For each measurement, the sample was cooled from 390 K to the desired temperature in zero field. Low temperature thermal expansion measurements were performed by measuring the resistance change of a Kyowa strain gauge in the temperature range of 120–380 K. Temperature dependence of lattice parameters was studied by performing Synchrotron XRD at beamline BL-18B, Photon Factory, Japan. The data were collected at an energy of 15 keV at various temperatures ranging between 50 and 300 K. The obtained data were then analyzed using the FullProf Suite and the lattice constants were obtained. Local structures around the constituent atoms were investigated by x-ray absorption fine structure (XAFS) spectroscopy at the Mn–K and the Co–K edge at various temperatures ranging between 100 and 300 K on the P65 beamline at the PETRA III synchrotron source, DESY, Hamburg, Germany using a Si(111) double crystal monochromator and two Si mirrors at an angle of incidence of 2 mrad for higher harmonics suppression, a standard configuration for this energy range.[56] Absorbers were made by stacking $20 \times 5\,mm^2$ strips of scotch tape, uniformly coated with very fine sample powder (~20 μm). The thickness of the absorbers was adjusted to limit the total absorption to ≤ 2.5 beyond the absorption edge. The incident and the transmitted photon beam intensities were measured using ionization chambers filled with the appropriate gases. At least three scans were recorded at every temperature and averaged to reduce the statistical noise. Data analysis was done using the DEMETER suite.[57]

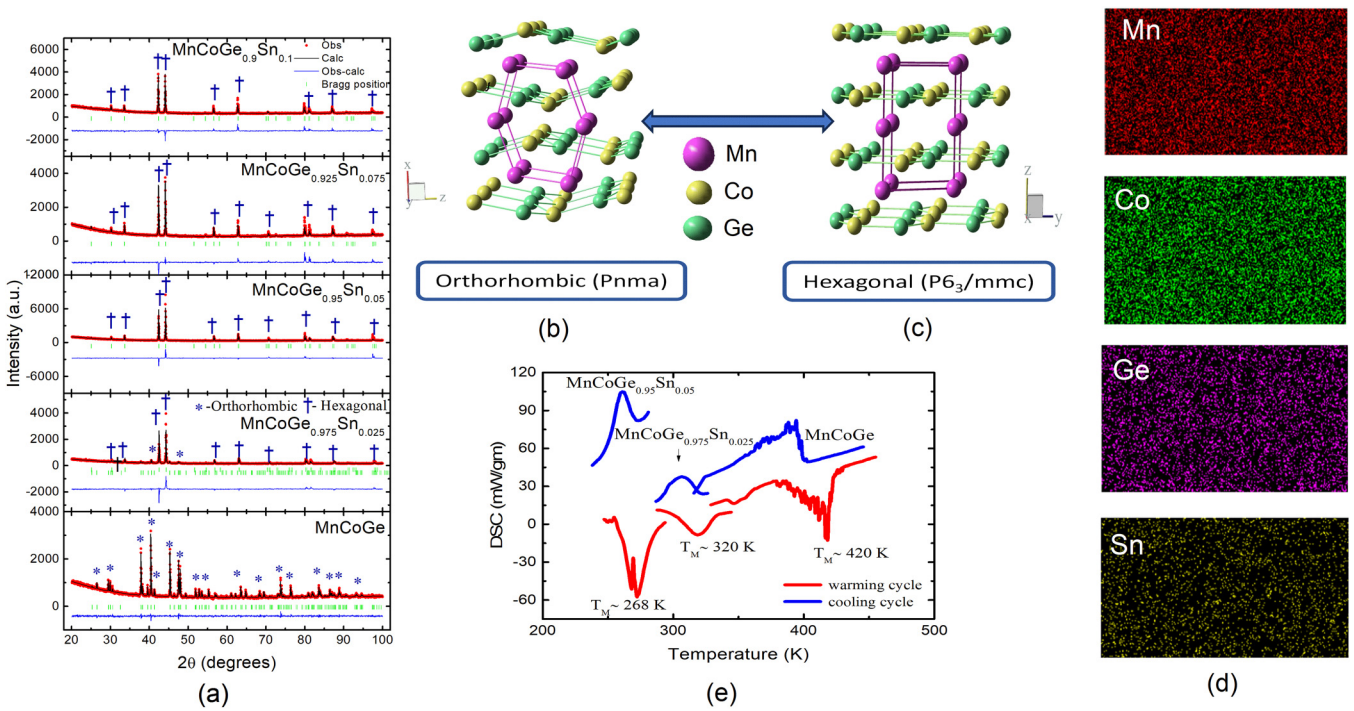

FIG. 1. (a) Rietveld refined x-ray diffraction plots for $MnCoGe_{1-x}Sn_x$ ($x = 0$, 0.025, 0.05, 0.075, 0.1) alloys. Crystal structure of MnCoGe in the (b) orthorhombic and (c) hexagonal phases. (d) False color maps depicting the Mn, Co, Ge, and Sn homogeneity for the $MnCoGe_{0.9}Sn_{0.1}$ sample. (e) DSC thermograms for MnCoGe, $MnCoGe_{0.975}Sn_{0.025}$, and $MnCoGe_{0.95}Sn_{0.05}$ during the warming and the cooling cycles.

III. RESULTS

Figure 1(a) displays the Rietveld refined x-ray diffraction patterns of all the samples recorded at room temperature. Since the martensitic transition temperature (T_M) of MnCoGe, ($x = 0$) is well above room temperature, it crystallizes in the TiNiSi-type orthorhombic structure (Space Group: *Pnma*) shown in Fig. 1(b). The diffraction pattern of $x = 0.025$ primarily contains peaks of the Ni_2In-type hexagonal phase ($P6_3/mmc$) along with weak reflections arising from the orthorhombic phase, indicating that its T_M is around room temperature. Alloy compositions with higher Sn concentration, $x = 0.05$, 0.075, and 0.1, display a hexagonal Ni_2In-type structure [Fig. 1(c)]. The lattice constants obtained from Rietveld refinement agree well with previous work[58–60] and are listed in Table I. The systematic increase in the lattice constants of the hexagonal phase with increasing Sn content can be ascribed to the substitution of the larger Sn ($r = 1.58$ Å) for Ge ($r = 1.22$ Å).

Further confirmation of the alloy compositions was obtained from SEM-EDS. The elemental false color maps depicted for $x = 0.1$ in Fig. 1(d) confirm the homogeneous nature of the alloy with no evident phase segregation. The average composition is determined by scanning an area of 100 μm^2 of the sample and that obtained from three randomly selected spots within this area agree

TABLE I. Room temperature lattice parameters and EDS compositions of $MnCoGe_{1-x}Sn_x$ alloys.

	Orthorhombic			Hexagonal		
Alloy	a (Å)	b (Å)	c (Å)	a (Å)	c (Å)	EDS composition
MnCoGe	5.9417	3.8201	7.0487	…	…	$Mn_{1.02}Co_{1.02}Ge_{0.96}$
$MnCoGe_{0.975}Sn_{0.025}$	5.9299	3.8287	7.0587	4.0880	5.3132	$Mn_{1.00}Co_{1.02}Ge_{0.96}Sn_{0.02}$
$MnCoGe_{0.95}Sn_{0.05}$	…	…	…	4.1033	5.3325	$Mn_{1.04}Co_{1.00}Ge_{0.93}Sn_{0.03}$
$MnCoGe_{0.925}Sn_{0.075}$	…	…	…	4.1063	5.3367	$Mn_{1.02}Co_{1.02}Ge_{0.91}Sn_{0.05}$
$MnCoGe_{0.9}Sn_{0.1}$	…	…	…	4.1103	5.3453	$Mn_{1.00}Co_{1.00}Ge_{0.92}Sn_{0.08}$

well with each other and are within ~ 3% of the nominal composition of the alloys. Table I lists the SEM-EDS composition of the alloys.

Figure. 1(e) shows the DSC curves for the $MnCoGe_{1-x}Sn_x$ alloys recorded at a rate of 5 K/min during the warming and cooling cycles. Strong exothermic and endothermic peaks in $x = 0$, 0.025, and 0.05 accompanied by a hysteretic behavior confirm the presence of a first order transition in these compounds. MnCoGe undergoes a structural transformation from the hexagonal to the

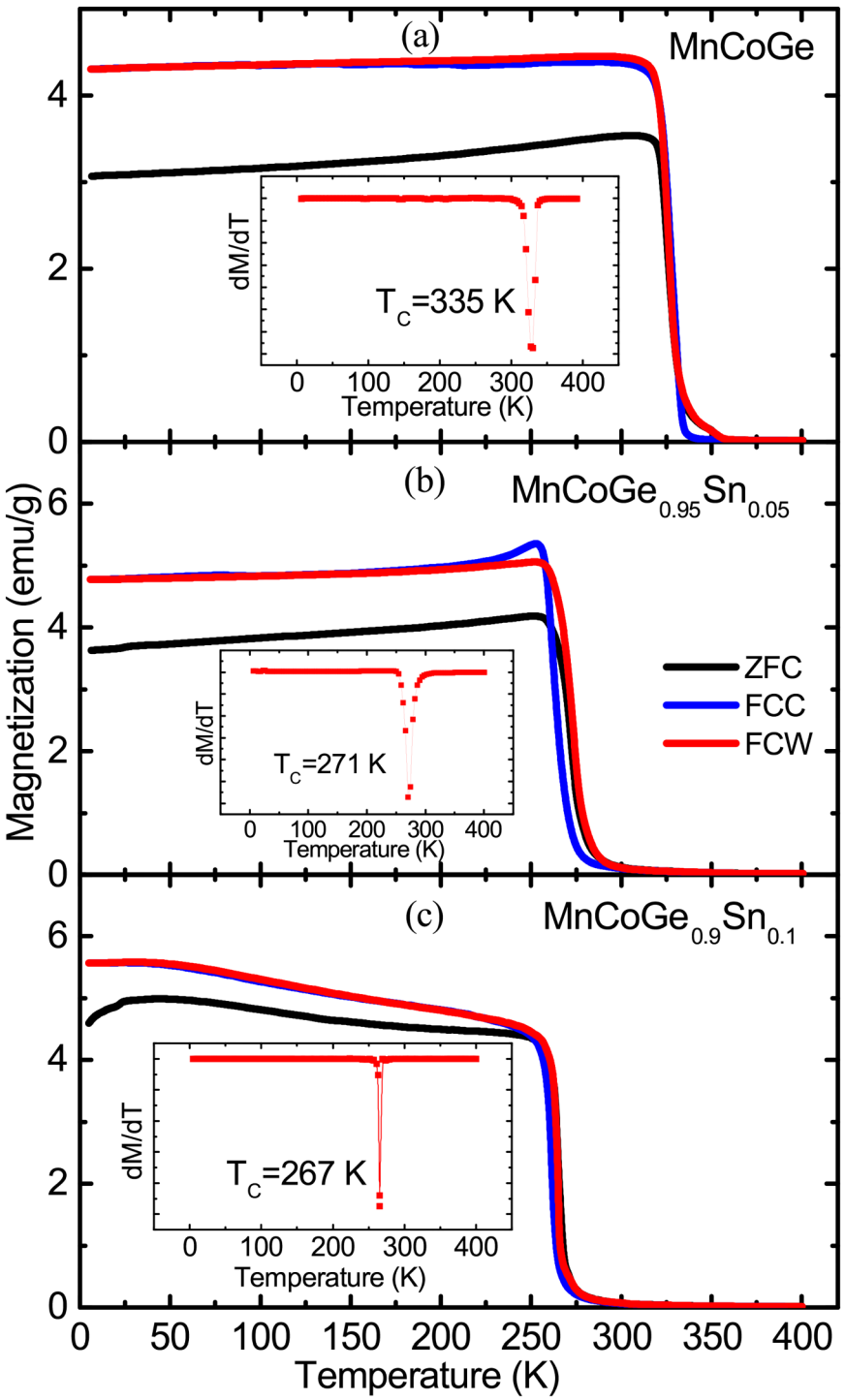

FIG. 2. Magnetization M(T) recorded in the temperature range 5 K $\leq T \leq$ 400 K during ZFC, FCC, and FCW cycles in the applied field of 100 Oe for MnCoGe, $MnCoGe_{0.95}Sn_{0.05}$, and $MnCoGe_{0.9}Sn_{0.1}$ alloys.

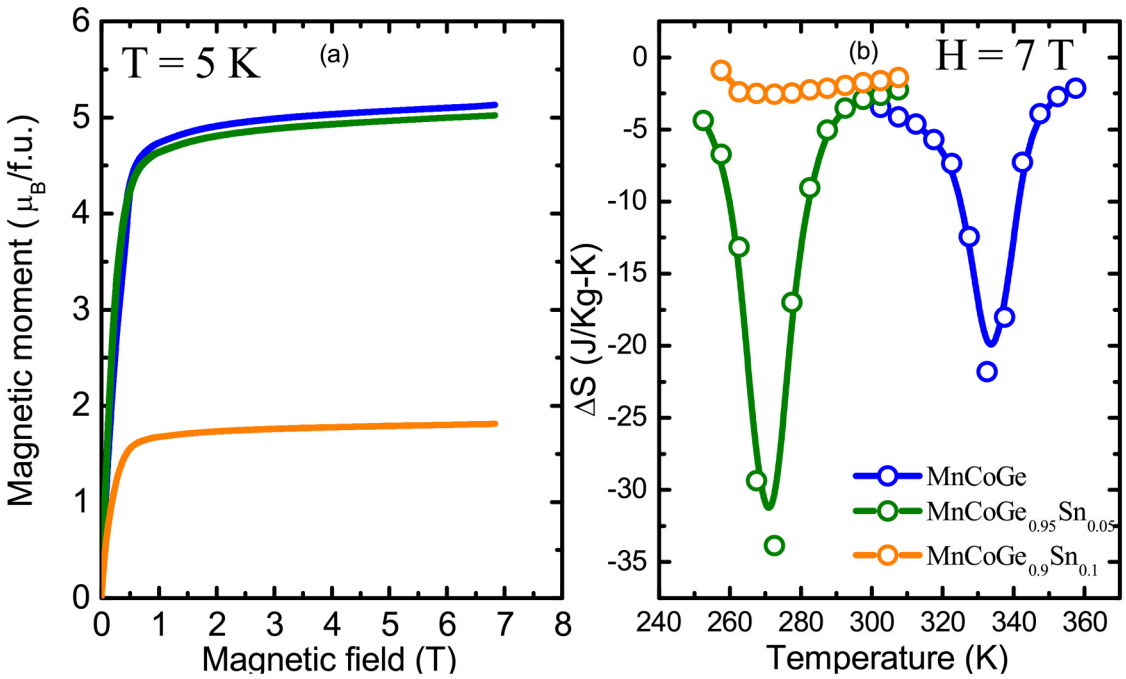

FIG. 3. (a) Isothermal magnetization curves M(H) recorded at 5 K in the field range of 0 T $\leq H \leq$ 7 T for MnCoGe, $MnCoGe_{0.95}Sn_{0.05}$, and $MnCoGe_{0.9}Sn_{0.1}$ alloys. (b) Entropy change associated with the magnetic transition in MnCoGe, $MnCoGe_{0.95}Sn_{0.05}$, and $MnCoGe_{0.9}Sn_{0.1}$ alloys.

orthorhombic phase at around 420 K while warming and around 394 K while cooling.[61] Introduction of Sn at the Ge site reduces the T_M to around 320 K while warming and 308 K while cooling in $MnCoGe_{0.975}Sn_{0.025}$. A further increase in Sn concentration to $x = 0.05$ reduces the T_M to around 268 K while warming and 262 K while cooling. No phase transition was observed in DSC for $x = 0.075$ and 0.1 (supplementary material). Resistivity measurements down to 30 K (supplementary material) also did not show the presence of any phase transition in these two alloys.

Magnetization as a function of temperature, M(T) recorded in the ZFC, FCC, and FCW protocols under an applied field of 0.01 T for MnCoGe, $MnCoGe_{0.95}Sn_{0.05}$, and $MnCoGe_{0.9}Sn_{0.1}$ is presented in Figs. 2(a)–2(c). The paramagnetic to ferromagnetic transition temperatures T_C in each of the alloys were determined from the minimum in dM/dT curves (shown as insets for all the samples). The T_C for MnCoGe is found to be 335 K, which is below its $T_M = 420$ K in agreement with previous reports.[33,49,51,58] With 5% substitution of Sn for Ge, the magnetic ordering temperature reduces and coincides with the martensitic transition temperature, indicating magnetostructural coupling and hence is represented by $T_{ms} = 271$ K determined from the DSC measurements. The distinct hysteresis between the FCC and FCW magnetization curves also indicates the first order nature of the magnetic transition. $MnCoGe_{0.9}Sn_{0.1}$ undergoes PM to FM transition at $T_C = 267$ K. The absence of any hysteresis between FCC and FCW magnetization curves indicates the transition to be second order type. The absence of any structural phase transition is also confirmed from DSC and resistivity measurements performed on this alloy (supplementary material). Another aspect to be noted from M(T) measurements is the bifurcation between ZFC and FC magnetization curves. This could be ascribed to the random magnetization of domains in zero field conditions and their correlated orientation under the influence of the field. The presence of magnetic inhomogeneities also results in such a behavior.

Isothermal magnetization curves were recorded at 5 K for the field interval of 0–7 T and the same are presented in Fig. 3(a). While the magnetic moment values in MnCoGe and $MnCoGe_{0.95}Sn_{0.05}$ are nearly same ($\sim 4.8 \mu_B/f.u.$) and in agreement with the literature reports,[62] it decreases sharply to 1.7 μ_B/f.u. in the case of $MnCoGe_{0.9}Sn_{0.1}$ alloy. It is well known that both Mn and Co carry a magnetic moment in the orthorhombic phase while only Mn atoms possess an ordered moment in the hexagonal phase of MnCoGe.[63] This could well be the reason for the lower magnetic moment in $MnCoGe_{0.9}Sn_{0.1}$. However, the magnetic moment value observed in $MnCoGe_{0.9}Sn_{0.1}$ is lower than 2.3 $\mu_B/f.u.$ reported for hexagonal MnCoGe.[63]

The entropy change at the magnetic phase transition is often used as a measure of magnetostructural coupling in the alloys. To understand the effect of Sn doping in MnCoGe on the magnetostructural coupling, entropy changes were calculated and the plots are presented in Fig. 3(b). The entropy change was calculated from the series of isothermal magnetization curves recorded every 5 K over a 60 K interval (supplementary material) about the T_C's of the

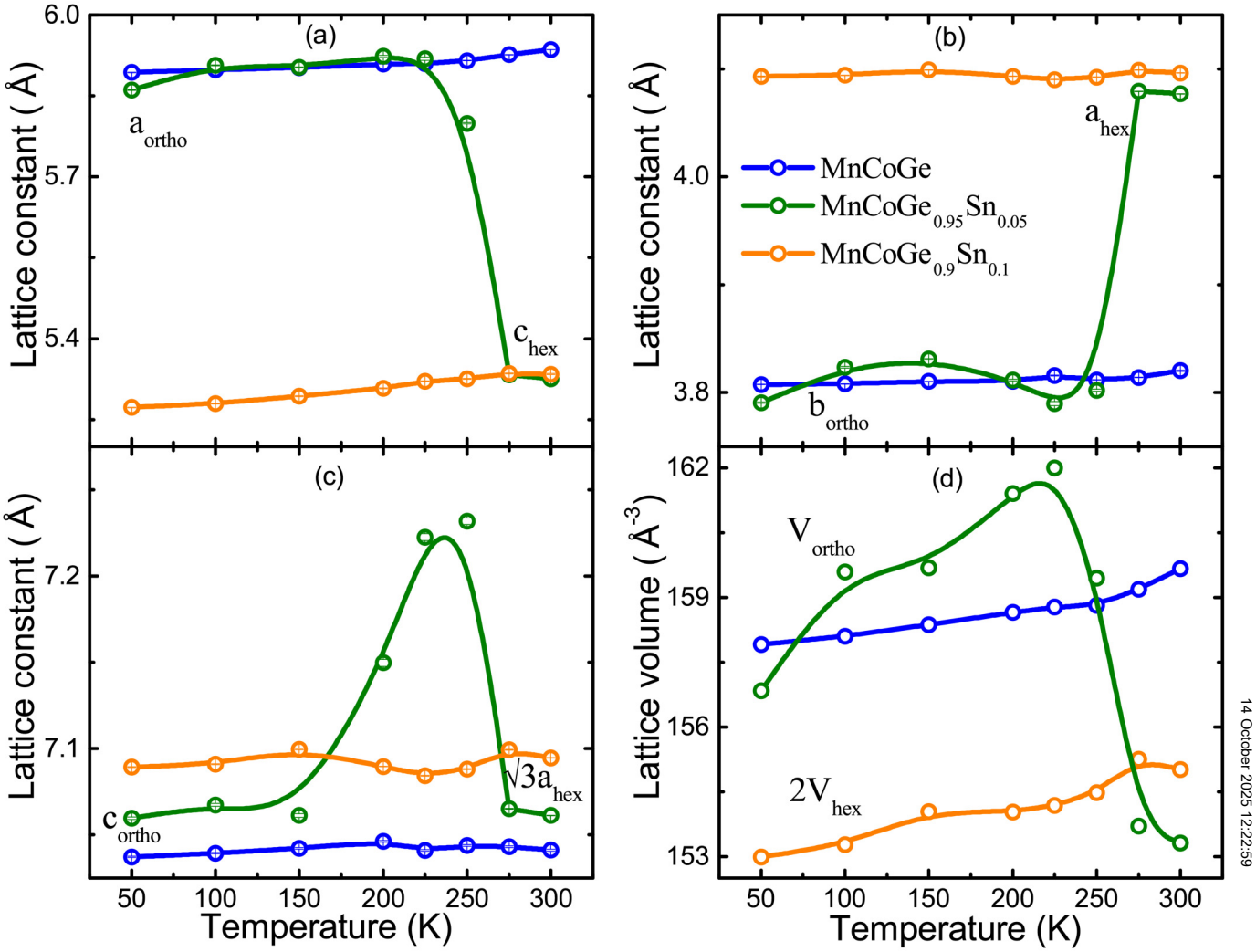

FIG. 4. Temperature variation of lattice constants *a*, *b*, and *c* and the unit cell volume, *V* for orthorhombic and hexagonal phases of MnCoGe, $MnCoGe_{0.95}Sn_{0.05}$, and $MnCoGe_{0.9}Sn_{0.1}$ alloys.

respective alloys using Maxwell's equation

$$\Delta S = \int_0^{7T} \left(\frac{\partial M}{\partial T}\right)_H.$$

The entropy change in MnCoGe is ~20 J/kg K at its $T_c = 335$ K. This value increases to ~35 J/kg K at its $T_c = 270$ K in $MnCoGe_{0.95}Sn_{0.05}$.[31,64,65] This increase in the magnetostructural coupling is due to the coincidence of martensitic and magnetic transition in this alloy. Surprisingly, the value of ΔS decreases sharply to ~3 J/kg K in $MnCoGe_{0.9}Sn_{0.1}$, signifying the disappearance of magnetostructural coupling in this alloy.

Martensitic phase transition that drives the structure from the hexagonal austenitic phase to the orthorhombic martensitic phase is accompanied by a large negative thermal expansion. To investigate the structural changes in the Sn doped alloys, synchrotron x-ray diffraction measurements were performed as a function of temperature. Diffraction patterns were recorded during the warming cycle in the temperature interval of $50\,K \leq T \leq 300\,K$ for the three $MnCoGe_{1-x}Sn_x$ ($x = 0$, 0.05, and 0.1) compositions (supplementary material). As the martensitic transition temperature of MnCoGe is 420 K, the diffraction patterns in $50\,K \leq T \leq 300\,K$ interval could be indexed to the orthorhombic phase. In the case of $MnCoGe_{0.95}Sn_{0.05}$, the diffraction pattern at 300 K corroborates to the hexagonal phase. At 275 K, peaks belonging to the orthorhombic phase appear and below 250 K, the structure is entirely

orthorhombic, in agreement with DSC and magnetization measurements. In the case of $MnCoGe_{0.9}Sn_{0.1}$, the hexagonal phase appears to be stabilized down to 50 K again confirming the disappearance of structural transition in this alloy composition.

Crystallographically, the TiNiSi-type orthorhombic structure can be considered the distortion of the Ni_2In-type hexagonal structure and hence the unit cell parameters and the cell volume of the orthorhombic and hexagonal structures are related as $a_{ortho} = c_{hex}$, $b_{ortho} = a_{hex}$, $c_{ortho} = \sqrt{3}a_{hex}$, and $V_{ortho} = 2V_{hex}$. Figure 4 displays the temperature dependence of the lattice constants and the unit cell volume for MnCoGe, $MnCoGe_{0.95}Sn_{0.05}$, and $MnCoGe_{0.9}Sn_{0.1}$ obtained from Le Bail refinement of the diffraction patterns. The lattice constants of MnCoGe in the orthorhombic phase and $MnCoGe_{0.9}Sn_{0.1}$ in the hexagonal phase show a monotonic increase with temperature over the entire temperature range of measurement between 50 and 300 K. A characteristic discontinuity in the variation of the lattice constants and a sharp decrease in the unit cell volume of $MnCoGe_{0.95}Sn_{0.05}$ are observed at 275 K, indicating a negative thermal expansion. The negative thermal expansion window extends over a temperature interval of 50 K from about 225 K to about 275 K. A volume change of $\sim 5.3\%$ noted at the transition is greater than that observed in MnNiGe (2.68%) and MnCoGe (4.0%) alloys, indicating a considerable atomic displacement during the structural reconstruction. In the orthorhombic phase, the ferromagnetic order is related to the shorter Mn–Mn distance along the *c*-axis, which is equivalent to the *a*-axis in the hexagonal phase. The values of $c_{ortho} \equiv \sqrt{3}a_{hex}$ at low temperatures for all the three alloys scale with the observed values of T_C in these alloys. The sharp increase in $c_{ortho} \equiv \sqrt{3}a_{hex}$ at the phase transition followed by the decrease in the c_{ortho} along with an increase in a_{ortho} in the case of $x = 0.05$ alloy confirms the presence of strong magnetostructural coupling in this alloy. It may be noted that the absence of negative thermal expansion coincides well with the comparatively small entropy change in $MnCoGe_{0.9}Sn_{0.1}$.

Studies so far reveal that, initially, with Sn doping, the magnetostructural coupling strengthens which is reflected in the enhanced entropy change as well as larger negative thermal expansion. With a further increase in Sn content, the martensitic transition disappears completely resulting in a very small entropy change and no negative thermal expansion. To investigate the cause of such a behavior, local structures around Mn and Co atoms were studied as a function of temperature. EXAFS data at the Mn and Co K edges in the *k*-range of 3 $Å^{-1}$ to 14 $Å^{-1}$ were Fourier transformed to *R*-range and then fitted using the structural correlations based on the crystal structure of the alloys. Emphasis was on observing changes in Mn–Mn, Mn–Co, Mn–Ge, Co–Co, and Co–Ge correlations occurring in the *R*-range of 1–4.5 Å in the case of orthorhombic structure and 1–3.7 Å for the hexagonal structure. These structural correlations are listed in Table II. Lowering of symmetry from hexagonal to orthorhombic structure lifts the degeneracy of all the bonds except for the nearest Mn–Mn bond along the c-axis. The bond length of this Mn–Mn bond, however, increases from 2.664 to 3.085 Å. It may be pointed out that the doubly degenerate Mn–Mn bond at 4.769 Å was not used in the analysis as the upper limit of *R*=range for fitting Mn EXAFS data was set to 4.0 Å. The main reason for setting the limit was the presence of hardly any signal in the magnitude of Fourier transform (FT) beyond 4 Å due to too many scattering paths contributing out of phase with each other.

TABLE II. Type of bond, coordination no. (C.N.), and bond distance for MnCoGe in the orthorhombic and the hexagonal phases calculated from crystal structure and lattice parameters obtained from x-ray diffraction.

Orthorhombic			Hexagonal		
Type of bond	C.N.	Bond distance (Å)	Type of bond	C.N.	Bond distance (Å)
Mn–Mn	2	3.085	Mn–Mn	2	2.664
Mn–Mn	2	3.318	Mn–Mn	6	4.097
Mn–Mn	2	3.820			
Mn–Mn	2	4.769			
Mn–Ge	3	2.623	Mn–Ge	6	2.715
Mn–Ge	2	2.638			
Mn–Ge	1	3.4			
Mn–Co	1	2.691	Mn–Co	6	2.715
Mn–Co	3	2.817			
Mn–Co	2	2.841			
Co–Ge	2	2.320	$Co–Ge_{short}$	3	2.365
Co–Ge	1	2.376			
Co–Ge	1	2.376	$Co–Ge_{long}$	2	2.664
Co–Ge	1	3.629			
Co–Co	2	2.791	Co–Co	6	3.563
Co–Co	2	3.808			
Co–Co	2	4.014			

Figure 5 displays the FT magnitudes of Mn EXAFS in all the three samples. There are no directly visible changes in the FT magnitude due to the transformation from the hexagonal to orthorhombic structure. The local structure around Co as seen in Fig. 6 shows distinct changes due to structural transformation, especially in $MnCoGe_{0.95}Sn_{0.05}$. The first peak in the FT magnitude of Co EXAFS data appears to split into two upon the alloy transforming from orthorhombic to hexagonal structure at $T \geq 270$ K. The split first peak is also observed in the Co EXAFS data in *R* space at all temperatures in $MnCoGe_{0.9}Sn_{0.1}$. The absence of any other changes in the local structural features of Mn and Co EXAFS data corroborates the absence of Sn at the Mn or Co sites.

A structural model comprising all correlations mentioned in Table II with the exception of Mn–Mn bond at 4.769 Å was constructed to fit the Mn and Co EXAFS together. Appropriate structural constraints were employed to reduce the number of fitted parameters. The obtained fits were very good, and the fitted parameters obtained at each of the temperatures for MnCoGe, $MnCoGe_{0.95}Sn_{0.05}$, and $MnCoGe_{0.9}Sn_{0.1}$ are, respectively, given in the supplementary material. The FT magnitudes of Mn and Co EXAFS in the three alloys measured at 300 K, along with the respective fitted curves, are presented in Fig. 7.

The thermal evolution of Mn–Mn, Mn–Co, Mn–Ge, Co–Ge, and Co-Co bond distances is presented in Fig. 8. All the bond distances vary in accordance with the crystal structure. For instance, the two Mn–Mn bonds at ~2.65 and ~4.1 Å in the hexagonal phase split into a bunch of three distances, ~3.0, ~3.3, and ~3.8 Å and a much longer one at 4.7 Å in the orthorhombic phase. The

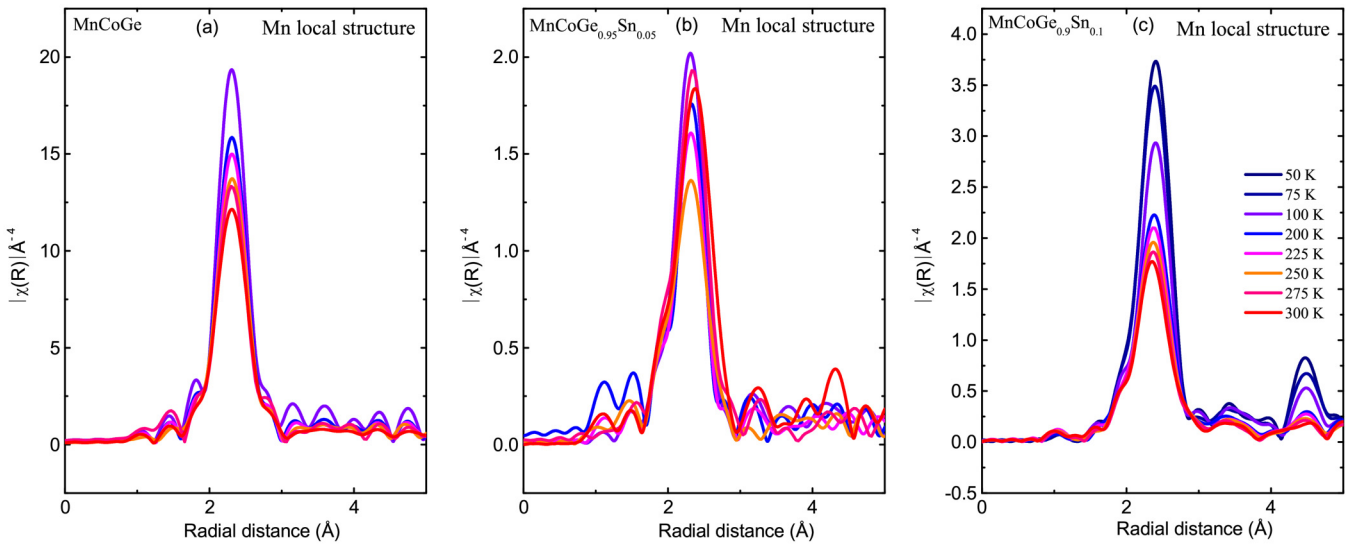

FIG. 5. Temperature evolution of the magnitudes of Fourier transform of Mn–K edge EXAFS data in (a) MnCoGe, (b) $MnCoGe_{0.95}Sn_{0.05}$, and (c) $MnCoGe_{0.9}Sn_{0.1}$ alloys.

Mn–Mn bond at 4.7 Å was not used in the fitting. A similar splitting is observed for other bond distances as well. These transformations are clearly seen in the case of $MnCoGe_{0.95}Sn_{0.05}$. As MnCoGe is orthorhombic in the entire temperature range studied here, only those sets of distances are observed from the EXAFS analysis. Similarly, only the hexagonal set of distances is observed in $MnCoGe_{0.9}Sn_{0.1}$.

IV. DISCUSSION

The hexagonal austenitic phase of MnCoGe adopts a layered structure composed of planar Co–Ge networks, in which the edge-sharing six-membered Co–Ge rings form a honeycomb structure stitched together by Mn atoms.[22] During the martensitic transformation to the orthorhombic phase, the Co–Ge layers undergo puckering causing a reconfiguration of Mn atoms such that they

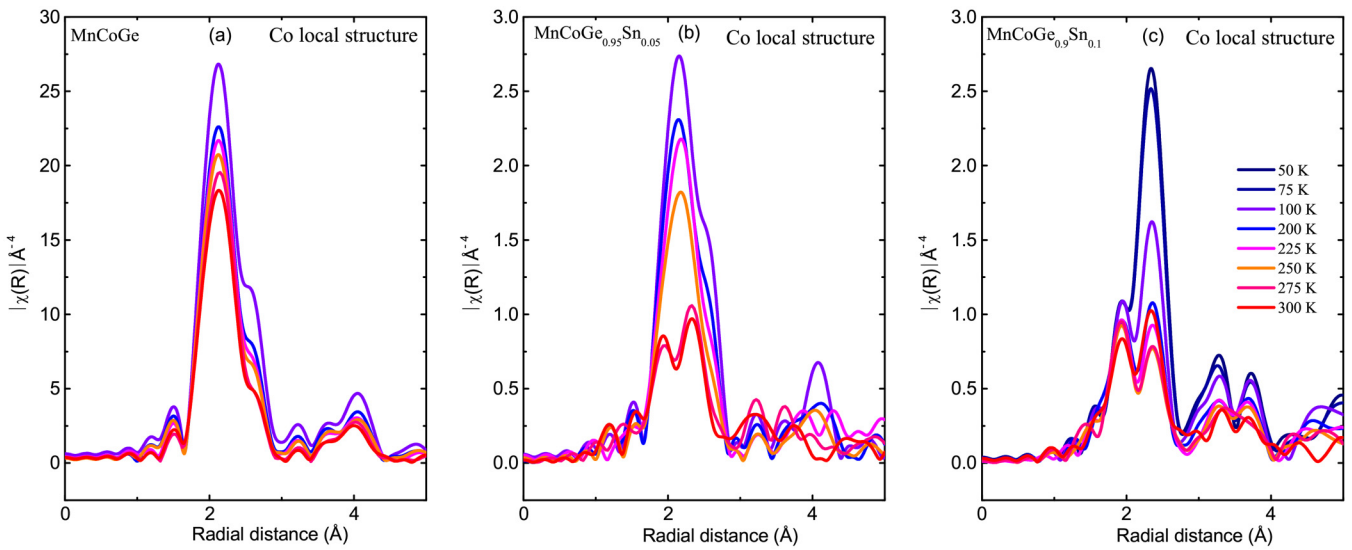

FIG. 6. Fourier transform magnitude of Co EXAFS as a function of temperature in (a) MnCoGe, (b) $MnCoGe_{0.95}Sn_{0.05}$, and (c) $MnCoGe_{0.9}Sn_{0.1}$ alloys.

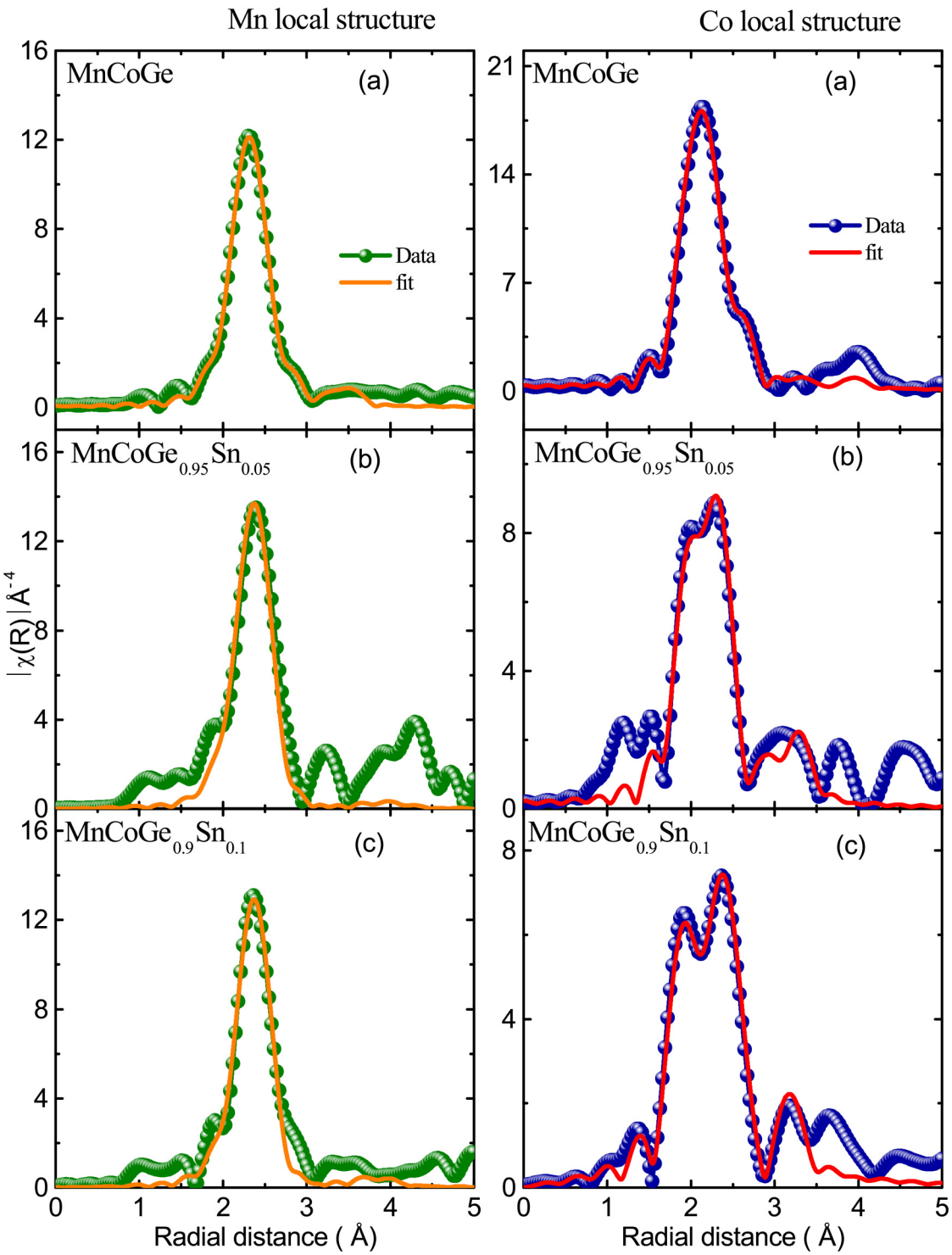

FIG. 7. Magnitude of Fourier transforms of k^3 weighted EXAFS data of Mn (left panel) and Co (right panel) K edges recorded at T = 300 K along with the best fit curves in (a) MnCoGe, (b) $MnCoGe_{0.95}Sn_{0.05}$, and (c) $MnCoGe_{0.9}Sn_{0.1}$ alloys.

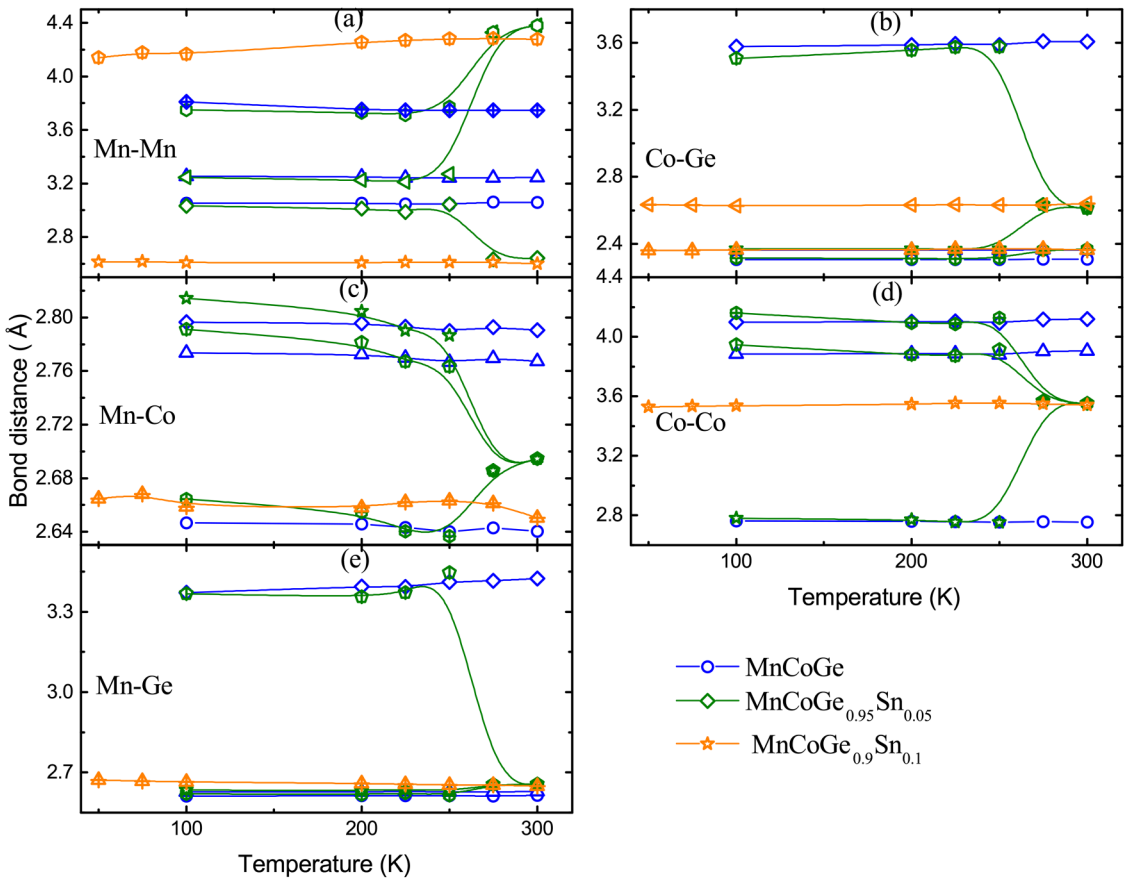

FIG. 8. Variation of Mn–Mn, Mn–Co, Mn–Ge, Co–Ge, and Co–Co bond distances as a function of temperature, obtained from Mn–K and Co–K EXAFS analysis in MnCoGe, $MnCoGe_{0.95}Sn_{0.05}$, and $MnCoGe_{0.9}Sn_{0.1}$ alloys.

come closer in the y–z plane of the orthorhombic lattice and simultaneously move apart along the x-axis.

Substitution of up to 10% Ge with larger Sn atoms in $MnCoGe_{1-x}Sn_x$ leads to a pronounced and systematic decrease of T_C and T_M. Notably at $x = 0.05$, the two transition temperatures converge, enhancing the magnetostructural coupling. The strong magnetostructural coupling is evidenced through a significantly larger change in the unit cell volume, a microscopic spin-phonon coupling elucidated by a jump in isothermal magnetization at $T \approx T_C$ (see Fig. S2 in the supplementary material) and enhanced entropy change across the transition relative to undoped MnCoGe. However, a further increase in Sn content to $x \geq 0.075$ results in a complete suppression of martensitic transformation along with the disappearance of the negative thermal expansion, the absence of the metamagnetic like transition at T_C, and a very small entropy change seen in $MnCoGe_{0.9}Sn_{0.1}$.

The pronounced structural changes lead to macroscopic changes in physical properties of Sn substituted alloys. The structural changes can be easily seen from global structural probes like XRD and local probes like EXAFS. Such large changes in the near neighbor environment of Mn and Co make it difficult to notice the relatively smaller changes due to Sn doping. In $MnCoGe_{1-x}Sn_x$ alloys, the local structures around Mn and Co confirm to the crystal structures of the alloys. This observation contrasts with full Heusler martensitic alloys such as Ni_2MnGa, wherein the local structural changes play a critical role in driving the martensitic transformation.[66–68] Such a contrasting observation between MnCoGe and other full Heusler martensitic alloys could be ascribed to the hexagonal structure of MnCoGe in the austenitic phase, which is of lower symmetry compared to the $L2_1$ structure of Ni_2MnGa-type alloys.

Further, though Sn substitution in MnCoGe does not alter the e/a ratio, similarities between the effect of applied pressure and Sn doping on T_C and T_M have been highlighted.[41] However, the present study shows a monotonic increase in the lattice parameters and similar changes in the local structure of Mn and Co with Sn doping, thereby questioning the hypothesis that Sn doping induces pressure-like effects on the Mn–Mn and Co–Ge bonding networks.

Analysis of the mean square variation in bond distance (σ^2) extracted from the EXAFS data provides additional light on the

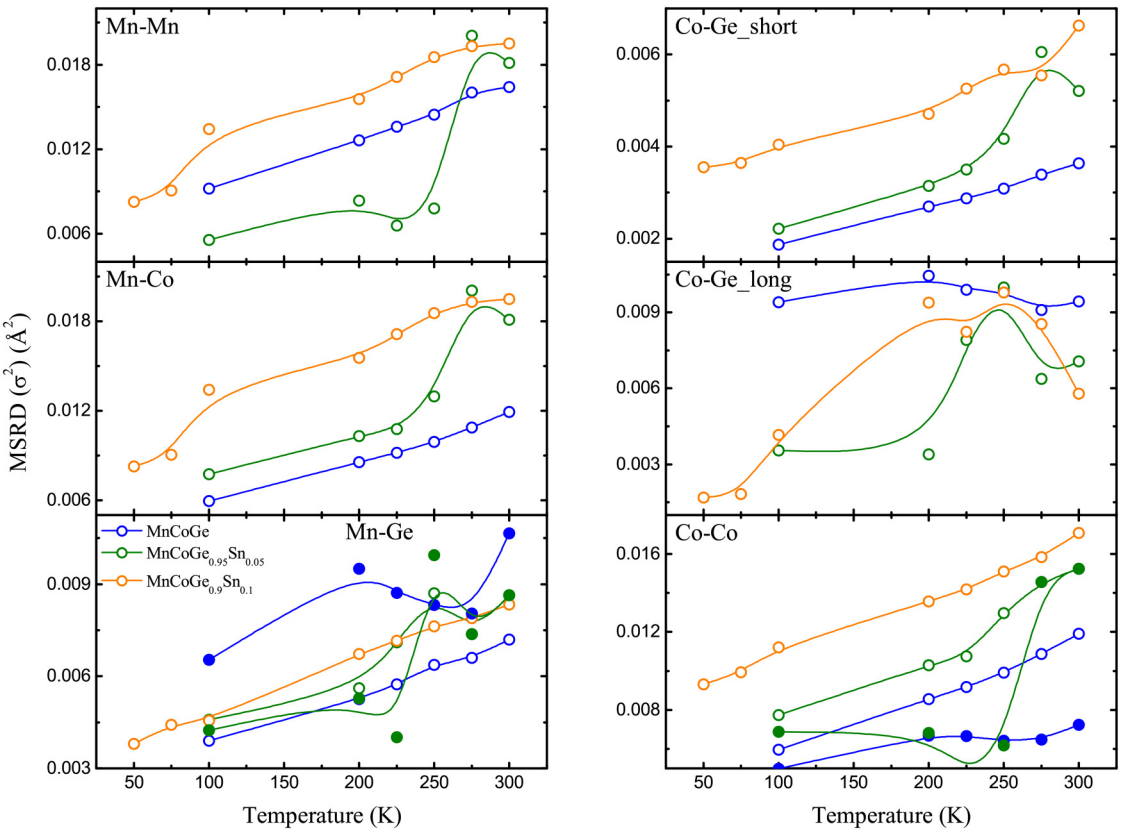

FIG. 9. Thermal evolution of mean square radial disorder (MSRD) in Mn–Mn, Mn–Co, Mn–Ge, Co–Ge, and Co–Co bond distances obtained from Mn–K and Co–K EXAFS analysis in MnCoGe, $MnCoGe_{0.95}Sn_{0.05}$, and $MnCoGe_{0.9}Sn_{0.1}$ alloys.

role of disorder. As can be seen from Fig. 9, except for Mn–Ge and Co–Ge bonds, the σ^2 values of Mn–Mn and Co–Co bonds increase systematically with Sn content. Considering that the thermal contribution to σ^2 to be similar across the $MnCoGe_{1-x}Sn_x$ series due to comparable lattice parameters, the observed increase in σ^2 primarily arises from the structural disorder. This interpretation is further corroborated by the random distribution of Sn in the alloy and the absence of any phase segregation as seen in the false color images presented in Fig. 1.

The structural disorder caused by Sn doping disrupts the long-range coherence of magnetic and structural interactions, leading to the observed decrease in magnetic and martensitic transformation temperatures. At low Sn concentrations, the coinciding transition temperatures enhance the magnetostructural coupling and amplify the associated magnetovolume and entropy changes. With a further increase in Sn content, the disorder increases and the coupling diminishes, which is reflected in the absence of negative thermal expansion and significant reduction in the entropy change at the magnetic transition in $MnCoGe_{0.9}Sn_{0.1}$.

Materials like LaFeSi exhibit an entropy change around 15 J/kg K under a magnetic field change (ΔH) of 2 T[69] while $Gd_5Si_2Ge_2$ displays an entropy change of 20 J/kg K under $\Delta H = 5$ T[70] but with an associated hysteresis of around 8 K. Comparatively, $MnCoGe_{0.95}Sn_{0.05}$ shows a large entropy change (~35 J/kg K under $\Delta H = 7$ T) with an associated hysteresis of 7 K, making it a promising MCE material. However, the large volume change associated with the magnetostructural transition can affect the mechanical stability during cycling.

V. CONCLUSIONS

In summary, the present detailed study of local structural and magnetic characterization of $MnCoGe_{1-x}Sn_x$ highlights the substitutional disorder introduced by Sn substitution in the Ge sublattice in MnCoGe. The disorder introduced by Sn disrupts the long-range correlated structural distortions driving the martensitic transformation and thereby resulting in a systematic decrease in both the T_M and the T_C. At low doping levels ($x \leq 0.05$), the convergence of T_M and T_C enhances magnetostructural coupling, thereby amplifying the MCE. However, further Sn substitution completely suppresses the martensitic transition, resulting in a breakdown of magnetostructural coupling and a diminished functional response.

SUPPLEMENTARY MATERIAL

The supplementary material consists of three figures and three tables. The three figures are (I) DSC thermograms, resistivity, and strain curves recorded for $MnCoGe_{0.925}Sn0.075$ and $MnCoGe_{0.9}Sn_{0.1}$; (II) isothermal magnetization curves used for entropy calculations in MnCoGe, $MnCoGe_{0.95}Sn_{0.05}$, and $MnCoGe_{0.9}Sn_{0.1}$; (III) synchrotron XRD profiles at selected temperatures and in the limited 2θ range to highlight the structure at room temperature and low temperatures. The three tables give local structural parameters obtained from Mn and Co EXAFS analysis in MnCoGe, $MnCoGe_{0.95}Sn_{0.05}$, and $MnCoGe_{0.9}Sn_{0.1}$, respectively.

ACKNOWLEDGMENTS

K.R.P. thanks the Council of Scientific and Industrial Research, New Delhi, for financial assistance under 03/1481/2023/EMR-II and the Department of Science and Technology, India for financial assistance under SR/PURSE/2023/198. The Department of Science and Technology, India and Jawaharlal Nehru Centre for Advanced Scientific Research, India are acknowledged for the travel support and facilitating the experiments at the Indian Beamline, Photon Factory, KEK, Japan and experiments at Petra III within the framework of India DESY collaboration. We acknowledge DESY (Hamburg, Germany), a member of the Helmholtz Association HGF, for providing experimental facilities. Parts of this research were carried out at Petra III using P65 beamline using the beamtime allocated for Proposal No. I-20210145. Facilities at the University Laboratory for Materials Characterization, Goa University are also gratefully acknowledged. M.A. thanks the DST INSPIRE Programme for the fellowship (No. IF 190174).

AUTHOR DECLARATIONS

Conflict of Interest

The authors have no conflicts to disclose.

Author Contributions

M. Azavedo: Data curation (equal); Formal analysis (equal); Investigation (equal); Methodology (equal); Validation (equal); Visualization (equal); Writing – original draft (equal). **E. T. Dias:** Data curation (equal); Formal analysis (equal); Methodology (equal); Validation (equal); Visualization (equal); Writing – review & editing (equal). **K. R. Priolkar:** Conceptualization (equal); Data curation (equal); Funding acquisition (equal); Methodology (equal); Project administration (equal); Resources (equal); Supervision (equal); Validation (equal); Visualization (equal); Writing – review & editing (equal).

DATA AVAILABILITY

The data that support the findings of this study are available from the corresponding author upon reasonable request.

REFERENCES

[1]K. Sandeman, R. Daou, S. Özcan, J. Durrell, N. Mathur, and D. Fray, Phys. Rev. B–Condens. Matter Mater. Phys. **74**, 224436 (2006).
[2]S. Lin, O. Tegus, E. Bruck, W. Dagula, T. Gortenmulder, and K. Buschow, IEEE Trans. Magn. **42**, 3776 (2006).
[3]N. Trung, L. Zhang, L. Caron, K. Buschow, and E. Brück, Appl. Phys. Lett. **96**, 172504 (2010).
[4]J. Wang, C. Tan, G. Liang, L. Zhao, W. Zhao, J. Li, J. Yang, X. Wang, and X. Tian, J. Mater. Res. Technol. **33**, 8611 (2024).
[5]C. Zhang, Z. Zhang, D. Wang, and Y. Hu, Phys. Chem. Chem. Phys. **27**, 2046 (2025).
[6]V. O. Dolocan, E. Assaf, O. Pilone, L. Patout, A. Charaï, K. Hoummada, M. Bertoglio, A. Portavoce, and S. Bertaina, J. Phys. D: Appl. Phys. **58**, 035001 (2024).
[7]R. Li, C. Xie, Y. Wang, B. Jin, J. Zhu, X. Tang, and G. Tan, Mater. Today Phys. **48**, 101573 (2024).
[8]X. Hao, Y. Zhao, X. Huang, K. Liu, B. Zhao, C. Zhang, J. Ma, F. Qian, X. Miao, Y. Kuang, H. Yan, Z. Li, L. Zuo, X. Tong, B. Yang, and Q. Ren, Acta Mater. **296**, 121241 (2025).
[9]Y.-Y. Zhao, F.-X. Hu, L.-F. Bao, J. Wang, H. Wu, Q.-Z. Huang, R.-R. Wu, Y. Liu, F.-R. Shen, H. Kuang *et al.*, J. Am. Chem. Soc. **137**, 1746 (2015).
[10]Y. Liu, K. Qiao, S. Zuo, H. Zhang, H. Kuang, J. Wang, F. Hu, J. Sun, and B. Shen, Appl. Phys. Lett. **112**, 012401 (2018).
[11]F. Shen, H. Zhou, F. Hu, J.-T. Wang, S. Deng, B. Wang, H. Wu, Q. Huang, J. Wang, J. Chen *et al.*, Mater. Horiz. **7**, 804 (2020).
[12]Q. Ren, W. Hutchison, J. Wang, A. Studer, G. Wang, H. Zhou, J. Ma, and S. J. Campbell, ACS Appl. Mater. Interfaces **11**, 17531 (2019).
[13]W. Jeitschko, Acta Crystallogr. B **31**, 1187 (1975).
[14]V. Johnson, Inorg. Chem. **14**, 1117 (1975).
[15]Q. Ren, "New materials for magnetic refrigeration: the magnetocaloric effect in MnCoGe-based intermetallics," Ph.D. thesis (School UNSW Sydney, 2016).
[16]Q.-B. Hu, Y. Hu, Y. Fang, D.-H. Wang, Q.-Q. Cao, Y.-T. Yang, J. Li, and Y.-W. Du, AIP Adv. **7**, 056430 (2017).
[17]R. Li, L. Wang, P. Miao, C. Xie, X. Tang, and G. Tan, J. Magn. Magn. Mater. **603**, 172224 (2024).
[18]S. Pal, C. Frommen, S. Kumar, B. Hauback, H. Fjellvåg, T. Woodcock, K. Nielsch, and G. Helgesen, J. Alloys Compd. **775**, 22 (2019).
[19]C. Zhang, Y. Nie, H. Shi, E. Ye, Z. Han, and D. Wang, J. Magn. Magn. Mater. **469**, 437 (2019).
[20]Y. Shen, Y. Liu, W. Yu, X. Ma, Z. Zhang, J. Lin, and X. Luo, Mater. Res. Express **4**, 116110 (2017).
[21]X. Si, Y. Liu, Y. Shen, W. Yu, X. Ma, Z. Zhang, Y. Xu, and T. Gao, Intermetallics **93**, 30 (2018).
[22]Q. Ren, W. D. Hutchison, J. Wang, A. J. Studer, and S. J. Campbell, Chem. Mater. **30**, 1324 (2018).
[23]S. Yang, Y. Song, X. Han, S. Ma, K. Yu, K. Liu, Z. Zhang, D. Hou, M. Yuan, X. Luo *et al.*, J. Alloys Compd. **773**, 1114 (2019).
[24]J. Liu, Y. You, I. Batashev, Y. Gong, X. You, B. Huang, F. Zhang, X. Miao, F. Xu, N. Van Dijk *et al.*, Phys. Rev. Appl. **13**, 054003 (2020).
[25]J. Shi, H. Zhang, I. Hidayah, B. Song, H. Yao, M. Yue, and Z. Altounian, AIP Adv. **10**, 025325 (2020).
[26]Y. Wang, V. Yannello, J. Graterol, H. Zhang, Y. Long, and M. Shatruk, Chem. Mater. **32**, 6721 (2020).
[27]X. Sun, Y. Huang, J. Wu, Y. Wu, T. Wu, and S. Zhao, J. Magn. Magn. Mater. **590**, 171663 (2024).
[28]R. Li, C. Xie, Y. Wang, B. Jin, J. Zhu, X. Tang, and G. Tan, Mater. Today Phys. **48**, 101573 (2024).
[29]R. G. Suarez, I. Betancourt, M. Lopez-Cruz, J. Zamora, J. S. Llamazares, and J. Matutes-Aquino, J. Alloys Compd. **1018**, 179170 (2025).
[30]X. Wang, H. Zhang, J. Shi, X. Zhang, and M. Yue, J. Alloys Compd. **1010**, 177849 (2025).
[31]H. Zhang, L. Bao, X. Zhang, Y. Sang, Y. Ding, J. Gao, D. Zhao, H. Zhang, M. Tian, Y. Bai *et al.*, Phys. Lett. A **545**, 130503 (2025).
[32]A. Waske, M. E. Gruner, T. Gottschall, and O. Gutfleisch, MRS Bull. **43**, 268 (2018).

[33]G. Li, E. Liu, H. Zhang, Y. Zhang, J. Chen, W. Wang, H. Zhang, G. Wu, and S. Yu, J. Magn. Magn. Mater. **332**, 146 (2013).
[34]E. Yüzüak, I. Dincer, Y. Elerman, I. Dumkow, B. Heger, and S. Y. Emre, J. Alloys Compd. **641**, 69 (2015).
[35]Z. Wang, P. Xiu, L. Huang, Z. Nie, J. Zeng, D. E. Brown, Y. Ren, and Y. Wang, J. Magn. Magn. Mater. **406**, 179 (2016).
[36]T. Samanta, I. Dubenko, A. Quetz, S. Stadler, and N. Ali, Appl. Phys. Lett. **101**, 242405 (2012).
[37]S. Ma, Y. Zheng, H. Xuan, L. Shen, Q. Cao, D. Wang, Z. Zhong, and Y. Du, J. Magn. Magn. Mater. **324**, 135 (2012).
[38]J. Zeng, Z. Wang, Z. Nie, and Y. Wang, Intermetallics **52**, 101 (2014).
[39]H. Zhang, Y. Li, E. Liu, K. Tao, M. Wu, Y. Wang, H. Zhou, Y. Xue, C. Cheng, T. Yan *et al.*, Mater. Des. **114**, 531 (2017).
[40]J. Lai, Z. Zheng, R. Montemayor, X. Zhong, Z. Liu, and D. Zeng, J. Magn. Magn. Mater. **372**, 86 (2014).
[41]J. Hamer, R. Daou, S. Özcan, N. Mathur, D. Fray, and K. Sandeman, J. Magn. Magn. Mater. **321**, 3535 (2009).
[42]Y. Wang, V. Yannello, J. Graterol, H. Zhang, Y. Long, and M. Shatruk, Chem. Mater. **32**, 6721 (2020).
[43]Z.-B. Yu, H.-B. Zhou, F.-X. Hu, J.-T. Wang, F.-R. Shen, L.-H. He, Z.-Y. Tian, Y.-H. Gao, B.-J. Wang, Y. Lin *et al.*, NPG Asia Mater. **16**, 51 (2024).
[44]R. Wu, L. Bao, F. Hu, J. Wang, X. Zheng, Y. Liu, J. Sun, and B. Shen, J. Appl. Phys. **115**, 17A911 (2014).
[45]R.-R. Wu, L.-F. Bao, F.-X. Hu, H. Wu, Q.-Z. Huang, J. Wang, X.-L. Dong, G.-N. Li, J.-R. Sun, F.-R. Shen *et al.*, Sci. Rep. **5**, 18027 (2015).
[46]T. Gao, M. Wu, N. Qi, T. Zhou, X. Luo, Y. Liu, K. Xu, V. V. Marchenkov, H. Dong, Z. Chen *et al.*, J. Alloys Compd. **753**, 149 (2018).
[47]F. Liang, F. Shen, Y. Liu, J. Li, K. Qiao, J. Wang, F. Hu, J. Sun, and B. Shen, AIP Adv. **8**, 056417 (2018).
[48]Y. Song, S. Chen, S. Ma, Z. Zhang, K. Liu, S. U. Rehman, K. Yang, H. Zeng, Y. Zhang, C. Chen *et al.*, J. Magn. Magn. Mater. **495**, 165865 (2020).
[49]L. Bao, F. Hu, R. Wu, J. Wang, L. Chen, J. Sun, B. Shen, L. Li, B. Zhang, and X. Zhang, J. Phys. D: Appl. Phys. **47**, 055003 (2014).
[50]X. Si, Y. Liu, X. Lu, W. Wang, W. Lei, J. Lin, T. Zhou, and Y. Xu, J. Appl. Phys. **119**, 215104 (2016).
[51]J. Lai, Z. Zheng, R. Montemayor, X. Zhong, Z. Liu, and D. Zeng, J. Magn. Magn. Mater. **372**, 86 (2014).
[52]D. Choudhury, T. Suzuki, Y. Tokura, and Y. Taguchi, Sci. Rep. **4**, 7544 (2014).
[53]R. Kainuma, Y. Imano, W. Ito, Y. Sutou, H. Morito, S. Okamoto, O. Kitakami, K. Oikawa, A. Fujita, T. Kanomata *et al.*, Nature **439**, 957 (2006).
[54]S. K. Pal, C. Frommen, S. Kumar, B. Hauback, H. Fjellvåg, and G. Helgesen, Mater. Des. **195**, 109036 (2020).
[55]X. Si, K. Zhou, R. Zhang, Y. Liu, and J. Qi, Phys. Lett. A **381**, 1693 (2017).
[56]E. Welter, R. Chernikov, M. Herrmann, and R. Nemausat, AIP Conf. Proc. **2054**, 040002 (2019).
[57]B. Ravel and M. Newville, J. Synchrotron Radiat. **12**, 537 (2005).
[58]E. Liu, W. Zhu, L. Feng, J. Chen, W. Wang, G. Wu, H. Liu, F. Meng, H. Luo, and Y. Li, Europhys. Lett. **91**, 17003 (2010).
[59]N. ul Hassan, F. Chen, M. Zhang, I. A. Shah, J. Liu, Y. Gong, G. Xu, and F. Xu, J. Magn. Magn. Mater. **439**, 120 (2017).
[60]L. Gao, Y. Feng, S. Hu, and X. Xin, Metals **12**, 1143 (2022).
[61]C. Zhang, D. Wang, Q. Cao, S. Ma, H. Xuan, and Y. Du, J. Phys. D: Appl. Phys. **43**, 205003 (2010).
[62]S. Kaprzyk and S. Niziol, J. Magn. Magn. Mater. **87**, 267 (1990).
[63]T. Kanomata, H. Ishigaki, K. Sato, M. Sato, T. Shinohara, F. Wagatsuma, and T. Kaneko, J. Magn. Soc. Jpn. **23**, 418 (1999).
[64]T. Poudel Chhetri, J.-H. Chen, D. P. Young, I. Dubenko, S. Talapatra, N. Ali, and S. Stadler, J. Appl. Phys. **135**, 215101 (2024).
[65]J. Wang, C. Tan, G. Liang, L. Zhao, W. Zhao, J. Li, J. Yang, X. Wang, and X. Tian, J. Mater. Res. Technol. **33**, 8611 (2024).
[66]P. Bhobe, K. Priolkar, and P. Sarode, Phys. Rev. B **74**, 224425 (2006).
[67]D. Lobo, K. Priolkar, P. Bhobe, D. Krishnamurthy, and S. Emura, Appl. Phys. Lett. **96**, 232508 (2010).
[68]R. Nevgi, K. Priolkar, L. Righi, M. Solzi, F. Cugini, E. Dias, and A. Nigam, J. Phys.: Condens. Matter. **32**, 505801 (2020).
[69]B.-Y. Song, Y.-Q. Han, J. Cheng, L. Gao, X. Jin, Z.-B. Sun, and J.-H. Huang, J. Alloys. Compd. **990**, 174398 (2024).
[70]S. Sharma, A. K. Patel, and P. Kumar, Mater. Today. Commun. **26**, 102091 (2021).